9

Selected applications

In this chapter we present some real-life problems that can be modeled by the eddy current equations. In some of these examples the time-harmonic eddy current system is used for numerical simulations, and a rich bibliography on the subject is available. However, we also include some applications where, to our knowledge, the eddy current model has not yet been used. We believe that it could be a more accurate description than the ones actually employed, and, using the method proposed in this book, it should be suitable for numerical simulations.

In the following we focus on the illustration of the physical phenomena; the descriptions do not pretend to be complete and fully detailed, but just to give a flavour of different technological problems that are related to low-frequency electromagnetism.

9.1 Metallurgical thermoelectrical problems

We consider in this section two kind of electromagnetic furnaces used in the metallurgical industry: induction heating systems and electric reduction furnaces. There is an increasing interest in numerical simulations as means to optimize the design and to improve the performances of these kind of electromagnetic devices. In an induction furnace the eddy currents generated within conductors and resistances lead to Joule heating; in an electric reduction furnace the charged material is directly exposed to an electric arc. In both cases the mathematical model for the behaviour of the furnace involves thermal and electromagnetic phenomena, that can be described through the coupling of the Maxwell equations and the heat transfer equation.

Normally the electromagnetic submodel is solved in the frequency domain and the effect of displacement currents can be neglected, thus leading to the time-harmonic eddy current problem analyzed in this book. The electromagnetic and the thermal problem are coupled for two reasons: the electromagnetic properties of the different materials, in particular the electric conductivity, depend on the temperature, and the Joule effect is one of the source terms in the heat transfer equation. Other phenomena can be also taken into account; for instance, hydrodynamic phenomena must be consid-

A. Alonso Rodríguez, A. Valli: Eddy Current Approximation of Maxwell Equations.

ered when melting a metal in an induction furnace, while mechanical effects play an important role on the design of the electrodes of a reduction furnace.

In the following we present two different industrial applications. The first is the modelization of a coreless induction furnace designed for melting and stirring, and the second the modelization of an electric reduction furnace for the production of silicon.

9.1.1 Induction furnaces

In this section we follow the presentation of the problem given by Bermúdez et al. [41] and Vázquez [240]. Induction furnaces are widely used in metallurgical industry for hardening, melting or casting. An induction heating system is basically composed by an inductor, fed by an alternating electrical current, and a conducting object that has to be heated. More precisely, a coreless induction furnace for melting consists of a helical copper coil, connected to a power supply, and a workpiece formed by the crucible and the load within (see Figure 9.1). The alternating current traversing the inductor produces an oscillating magnetic field, which generates eddy currents. These currents, due to the Joule effect, produce heat in the conducting crucible, and the metal inside is also heated until it melts. The crucible is surrounded by refractory and insulating materials, and the inductor coil is water-cooled to avoid overheating due to Ohmic losses. The operating frequencies of the supplied alternating current may vary from utility frequency (50 or 60 Hz) to few kHz.

Numerical simulations are a valuable help in the shape optimization of this kind of system. There are many different aspects that must be taken into account for the design: the frequency and intensity of the applied current affect the temperature profile in the furnace and the stirring action within the molten metal, thus influencing the quality of the final product; ohmic losses could generate very high temperatures in the crucible, damaging it and reducing its lifetime; some physical parameters, such as the thermal and electrical conductivity of the refractory layer, and some geometrical parameters, as the crucible thickness or its distance from the coil, are also important for the performance of the device.

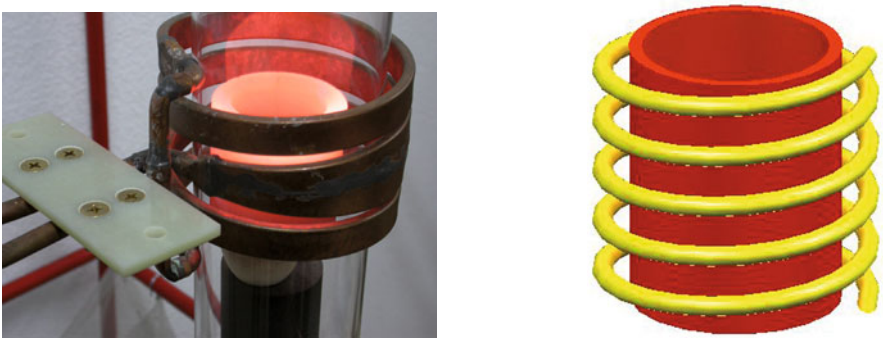

Fig. 9.1. An induction furnace (left, courtesy of V. Valcarcel, Ceramic Institute, Universidade de Santiago de Compostela) and a sketch of the computational geometry (right)

Melting systems were probably the first industrial application of eddy currents. Their modelization involves three main coupled phenomena: the electromagnetic field provides Joule heating and give rise to Lorentz forces that act on the molten metal.

Since the inductor is fed by an alternating current and the effect of the displacement current can be disregarded, the problem is modeled by the time-harmonic eddy current system

$$\begin{aligned} &\operatorname{curl} \mathbf{H} = \mathbf{J} \\ &\operatorname{curl} \mathbf{E} + i\omega \boldsymbol{\mu} \mathbf{H} = \mathbf{0} \,. \end{aligned}$$

The heating of the conductor due to the Joule effect is governed by the transient heat transfer equation with change of phase

$$\rho\Big(\frac{\partial e}{\partial t} + \mathbf{u} \cdot \operatorname{grad} e\Big) - \operatorname{div}(k \operatorname{grad} T) = \mathcal{J} \cdot \mathcal{E} \,,$$

where the heating due to viscous terms has been neglected, and e is the energy per unit mass, T the temperature, ρ the density, and k the thermal conductivity. The energy can be expressed as a multivalued function of the temperature, depending on different physical parameters. The right-hand side $\mathcal{J}(t, \mathbf{x}) \cdot \mathcal{E}(t, \mathbf{x})$ is the heat generated by eddy currents ($\mathcal{J}(t, \mathbf{x})$ and $\mathcal{E}(t, \mathbf{x})$ are the time-dependent total current density and electric field, respectively). The term $\mathbf{u} \cdot \operatorname{grad} e$ corresponds to the convective heat transfer; $\mathbf{u}$ is the velocity of the molten metal and it is given by the Navier-Stokes equations

$$\begin{aligned} &\rho \left(\frac{\partial \mathbf{u}}{\partial t} + (\mathbf{u} \cdot \operatorname{grad}) \mathbf{u} \right) - \operatorname{div}(2\eta D(\mathbf{u})) + \operatorname{grad} p = \mathbf{f}_g + \mathbf{f}_l \\ &\operatorname{div} \mathbf{u} = 0 \,, \end{aligned}$$

where η is the viscosity, p the pressure of the molten metal, and $D(\mathbf{u})$ the symmetric part of grad $\mathbf{u}$, namely,

$$D(\mathbf{u}) := \frac{\operatorname{grad} \mathbf{u} + (\operatorname{grad} \mathbf{u})^T}{2} \,.$$

The forces at the right-hand side of the Navier-Stokes equations are the buoyancy force $\mathbf{f}_g$, given by

$$\mathbf{f}_g = \rho \, \mathbf{g} \,,$$

where $\mathbf{g}$ is the acceleration of gravity, and the Lorentz force $\mathbf{f}_l$, given by

$$\mathbf{f}_l = \mathcal{J} \times \mathcal{B} \,,$$

where $\mathcal{B}(t, \mathbf{x})$ is the time dependent magnetic induction.

The heat source and the Lorentz force are determined taking the mean value on a cycle. Taking into account that $\mathcal{J}(t, \mathbf{x}) = \operatorname{Re}[e^{i\omega t} \mathbf{J}(\mathbf{x})]$ and analogously $\mathcal{E}(t, \mathbf{x}) = \operatorname{Re}[e^{i\omega t} \mathbf{E}(\mathbf{x})]$ and $\mathcal{B}(t, \mathbf{x}) = \operatorname{Re}[e^{i\omega t} \mathbf{B}(\mathbf{x})]$, an easy computation gives

$$\begin{aligned} &\tfrac{\omega}{2\pi} \textstyle\int_0^{2\pi} \mathcal{J}(t, \mathbf{x}) \cdot \mathcal{E}(t, \mathbf{x}) \, dt \\ &\quad = \tfrac{1}{2} \left(\operatorname{Re} \mathbf{J}(\mathbf{x}) \cdot \operatorname{Re} \mathbf{E}(\mathbf{x}) + \operatorname{Im} \mathbf{J}(\mathbf{x}) \cdot \operatorname{Im} \mathbf{E}(\mathbf{x}) \right) , \end{aligned}$$

and

$$\frac{\omega}{2\pi}\int_0^{2\pi}\mathcal{J}(t,\mathbf{x})\times\mathcal{B}(t,\mathbf{x})\,dt = \tfrac{1}{2}\left(\operatorname{Re}\mathbf{J}(\mathbf{x})\times\operatorname{Re}\mathbf{B}(\mathbf{x})+\operatorname{Im}\mathbf{J}(\mathbf{x})\times\operatorname{Im}\mathbf{B}(\mathbf{x})\right).$$

It should be noted that the Ohm law for a moving conductor reads

$$\mathbf{J}=\boldsymbol{\sigma}(\mathbf{E}+\mathbf{u}\times\mathbf{B}).$$

However, when working with molten metals on a laboratory scale, the term $\boldsymbol{\sigma}(\mathbf{u}\times\mathbf{B})$ can be neglected.

In most numerical schemes the coupled problem is solved using an iterative time stepping procedure, in which the electromagnetic field is first determined for temperature dependent conductivity and permeability, then the momentum and the temperature equations are advanced using the resulting Lorentz force and Joule loss distribution, and finally the material properties are updated and another step can be applied. Proceeding in this way, at each time step it is necessary to solve an eddy current problem like the one analyzed in the previous chapters of this book.

There is a very rich literature on numerical modeling of induction heating, and we refer to Lavers [163] for an extensive bibliographic review on this subject. More often, taking advantage of some geometrical symmetries, in many works concerning the coupling of electromagnetic and thermal problems the computational domain is two-dimensional. For instance, Chaboudez et al. [78] consider a two-dimensional problem involved in induction heating of long workpieces; Chaboudez et al. [77] do the same for an axisymmetric configuration; Bermúdez et al. [40] study the thermo-electromagnetic problem in induction furnaces used for melting, proposing and analyzing a FEM/BEM method for the approximation of the electromagnetic subproblem; Bay et al. [35] consider a model which couples electromagnetic, thermal and mechanical effects in axisymmetrical induction heating processes; Henneberger et al. [124], Natarajan and El-Kaddah [183] deal with the magneto-hydrodynamic problem in the context of induction melting systems with axisymmetric geometry, but they do not take explicitly into account thermal effects. Let us also mention Rappaz and Touzani [203] for the numerical analysis of a two-dimensional magneto-hydrodynamic problem.

By contrast, there are few works concerning the numerical approximation of the thermal-magneto-hydrodynamic problem: we mention the results by Henneberger and Obrecht [123], Katsumura et al. [149], and in particular the more recent paper by Bermúdez et al. [41] (see also Vázquez [240]); in all these works the axisymmetric geometry is assumed. More specifically, in Bermúdez et al. [41] and Vázquez [240] a BEM/FEM method is used for the approximation of the solution of the electromagnetic problem. The problem is formulated in terms of a magnetic vector potential and the input data of the problem are the current intensities through the inductor coils. Some numerical simulations for an industrial furnace are presented, and show a good agreement with experimental data. In this modelization, the induction coil has been replaced by a suitable set of rings, each one having toroidal geometry (see Figure 9.2).

As far as we know, there are no three-dimensional simulations of the thermal-magneto-hydrodynamic problem for the more realistic situation in which the coil is a

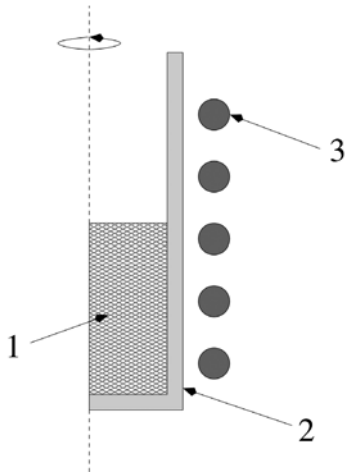

Fig. 9.2. Axisymmetric induction furnace: 1 metal, 2 crucible, 3 coils

simply-connected helix with two electric ports (for this type of coils in Section 8.1 we have presented a complete analysis of the eddy current problem).

9.1.2 Metallurgical electrodes

The time-harmonic eddy current model is also used in modeling the thermoelectrical behaviour of electrodes for electric reduction furnaces. Although the model is rather general, we focus on metallurgical electric furnaces for silicon metal and ferro-silicon production, following the presentation in Bermúdez et al. [43] (see also Bermúdez et al. [45], Salgado [217]). This kind of furnace basically consists of a cylindrical pot containing charged material and three electrodes symmetrically disposed. The pot is a steel cylinder charged with quartz and quartzite, as silicon oxide source, and carbonaceous substance, as coal and coke. At temperatures over 1900 degrees the carbon reduces the silica to silicon by the chemical reaction $SiO_2 + 2C \rightarrow Si + 2CO$. The electrodes are made of carbon materials and they serve to conduct the electric current to the center of the furnace. Different transformers change the high-voltage current usually supplied into the low-voltage high-intensity current suitable for the process. The electric current enters each electrode through a metal ring, which completely embraces the electrode above the charge level. The ring is composed by several copper sections, called contact clamps; bus bars connect the transformers to the contact clamps. At the tip of each electrode an electric arc is produced, generating the high temperatures that activate the chemical reaction. In Figure 9.3 we give a sketch of a reduction furnace.

The electrodes can be of different kinds, depending on the type of production, namely, silicon metal or ferro-silicon. Traditionally, in furnaces for silicon metal production two types of electrodes are mainly used: the pure graphite electrodes, composed by graphite bars joined by threated graphite connecting pieces, called nipples;

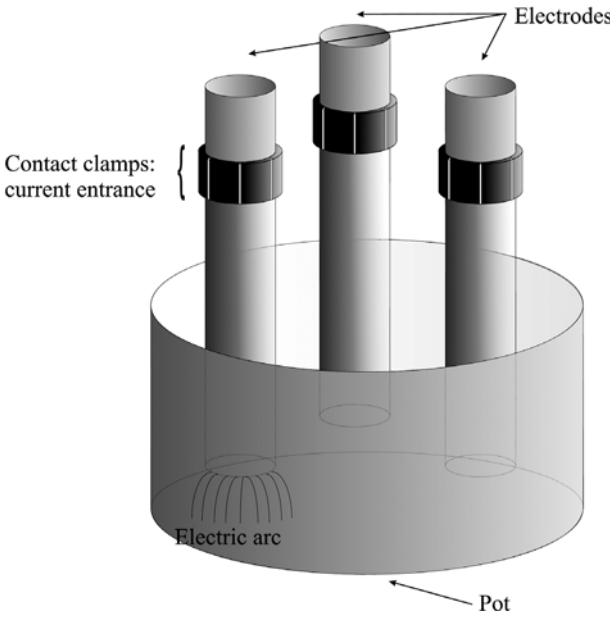

Fig. 9.3. Sketch of a reduction furnace (courtesy of A. Bermúdez, R. Rodríguez and P. Salgado)

the prebaked electrodes, composed by a mixture of carbonaceous substance known as paste, which has been previously baked to eliminate volatile substances.

Instead, the most used electrode in ferro-silicon industry is the Søderberg one, composed by a mixture of petroleum coke and coal-tar pitch contained into a steel cylinder. This paste is put in the cylinder at the top of the electrode, and it bakes in the zone of the contact clamps, employing the heat generated by the Joule effect. In this process the initially non-conductive paste at the top of the electrode becomes a solid carbon conductor. The baked electrode is consumed during the reaction that takes place at the tip of the pot, and has to be continuously replaced by pushing the carbon body down. This is done by moving the casing, but this procedure has the drawback that the steel melts and pollutes silicon. For this reason the Søderberg electrodes, that can be built in larger size and cost less than pure graphite or prebaked electrodes, are only used in the production of ferro-silicon, which can contain a large percentage of iron, but cannot be used to obtain pure silicon metal.

For many years graphite or prebaked electrodes have been the only kind of electrodes used in silicon metal production. In the early 1990s, the Spanish company Ferroatlántica S.L. built a new type of electrode named ELSA, that serves for the production of silicon metal at a lower cost. It consists of a central column of baked carbonaceous material, graphite or similar, surrounded by a Søderberg-like paste. There is a steel casing that contains the paste until it is baked, but the carbon core is responsible for slipping, so the casing does not move with the baked electrode and it does not melt. In this way it is possible to produce silicon with metallurgical quality. In Figure 9.4 we see a sketch of the ELSA electrode.

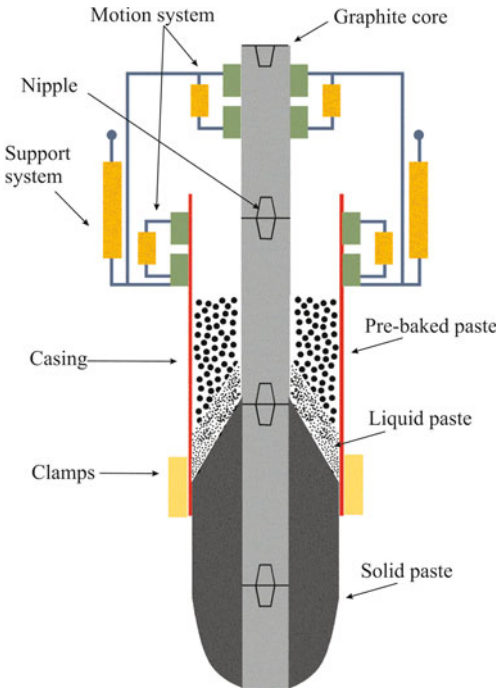

Fig. 9.4. Sketch of an ELSA electrode (courtesy of A. Bermúdez, R. Rodríguez and P. Salgado)

During the last decades many models and codes have been developed to simulate the working conditions of electric reduction furnaces. They compute the temperature distribution, the electromagnetic fields and the stress distribution inside the electrodes by solving the heat equation, the Maxwell equations and the elasticity equations. The system is coupled since the heat source depends on the electromagnetic fields, and the conductivity and stresses depend on the temperature. The alternating current and the low frequency (50 Hz) used make the eddy current model a good approximation for the electromagnetic submodel.

The early works concerning the modeling of a single electrode assume cylindrical symmetry (see, for instance, Bermúdez et al. [39]). The problem is solved in a vertical section of the electrode, writing the equations in cylindrical coordinates. Clearly, the two-dimensional model reduces the computational cost, but introduces some simplifications. Axisymmetric boundary conditions are assumed, but these are not realistic in industrial applications, for which the current enters the electrode through the contact clamps, and in each electrode half of the clamps is connected to one transformer while the others are connected to a second transformer. Moreover, the conductivity is not axisymmetric in the electrode, since it depends on the temperature, which is greater in the central part of the furnace containing the electrode.

There are few works concerning three dimensional simulation of metallurgical electrodes. The mathematical analysis of the continuous and the discrete problems in

the case of a single electrode can be found in Bermúdez et al. [46] for the $\mathbf{H}$-based formulation, and Bermúdez et al. [44] for the $\mathbf{E}$-based one. Notice that, in this case, the conductivity is assumed to be uniformly positive definite in the whole domain, and an insulating region is not present: the computational domain simply corresponds to the electrode and to the contact clamps. The problem is not axisymmetric, because it takes into account the non-symmetric boundary conditions that are typical in industrial applications.

Here we show some numerical simulations due to Bermúdez et al. [43] for an ELSA electrode. In Figures 9.5 we describe the geometrical configuration; in Figures 9.6, 9.7, 9.8 and 9.9 we show the magnitude of the current density in different sections of the electrode.

A delicate issue of the model that only considers one single electrode is the determination of the boundary conditions, as explained in Bermúdez et al. [44]. On the tip of the electrode, where the electric arc arises, the current exits freely, hence $\mathbf{E} \times \mathbf{n} = \mathbf{0}$. Also on the contacts, namely, the cross-sections of the bus bars through which the electric current enters the domain, the condition $\mathbf{E} \times \mathbf{n} = \mathbf{0}$ is imposed, and moreover the current intensity through each bus bar is known. Then one has $\mathbf{J} \cdot \mathbf{n} = 0$ outside the tip of the electrode and the contacts, since there is no current flux through this part of the boundary. Finally, $\boldsymbol{\mu}\mathbf{H} \cdot \mathbf{n}$ is set equal to 0 on the whole boundary, though this assumption is not valid in general: for instance, it is exactly true in the axisymmetric case, and it is admissible when the number of external bus bars feeding the electrode is large and they are arranged radially, because in this case the normal magnetic fluxes that they generate tend to cancel out. In more general situations one could take a larger domain around the electrode and the bus bars, and assign the boundary condition $\boldsymbol{\mu}\mathbf{H} \cdot \mathbf{n} = 0$ on

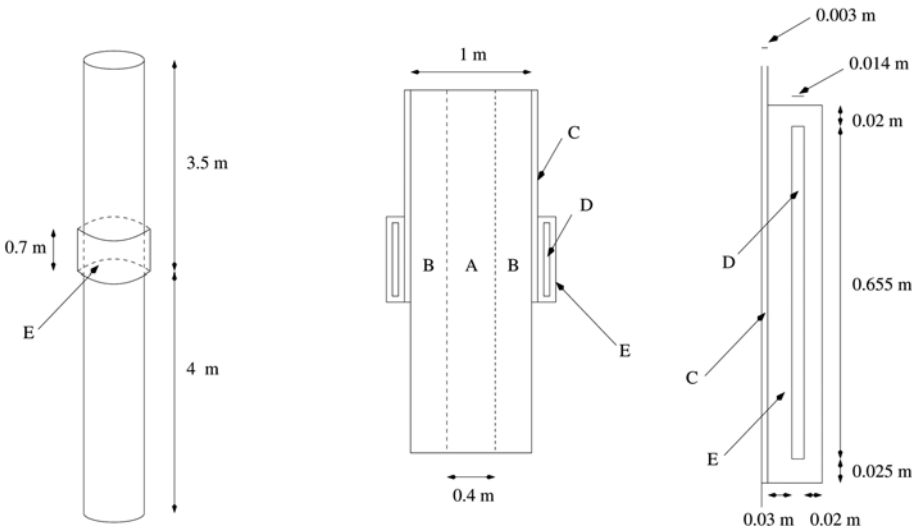

Fig. 9.5. The geometric configuration of the ELSA electrode: A graphite, B paste, C casing, D water, E contact clamp

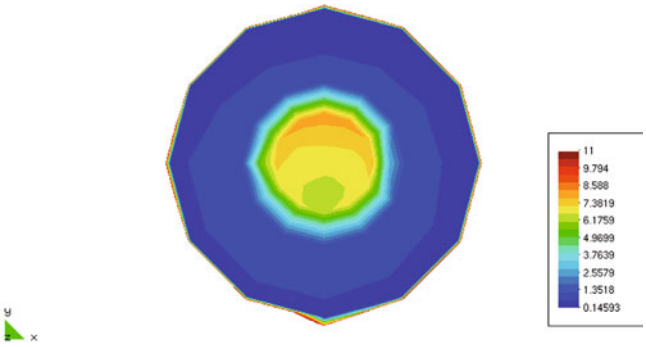

Fig. 9.6. Magnitude of the current density (A/cm^2): horizontal section at the top of contact clamps (courtesy of A. Bermúdez, R. Rodríguez and P. Salgado)

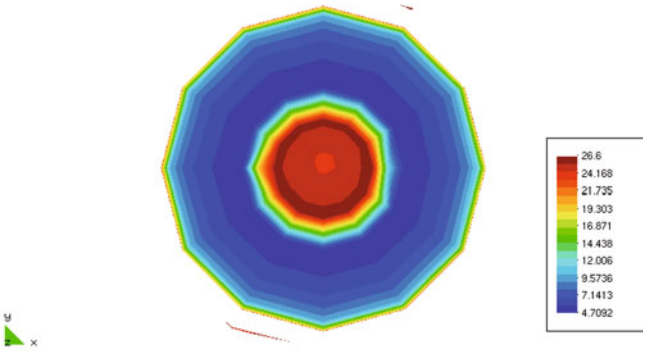

Fig. 9.7. Magnitude of the current density (A/cm^2): horizontal section at the bottom of contact clamps (courtesy of A. Bermúdez, R. Rodríguez and P. Salgado)

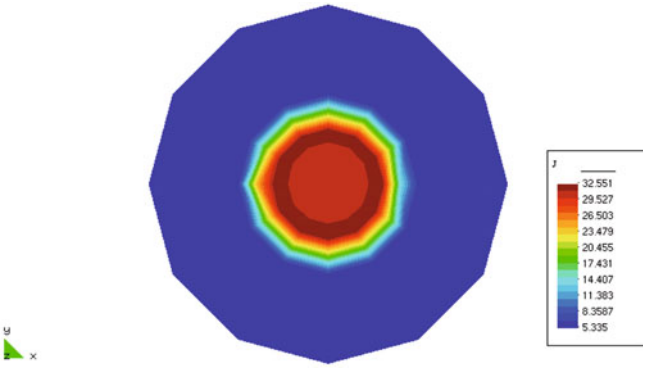

Fig. 9.8. Magnitude of the current density (A/cm^2): horizontal section 25 cm below the contact clamps (courtesy of A. Bermúdez, R. Rodríguez and P. Salgado)

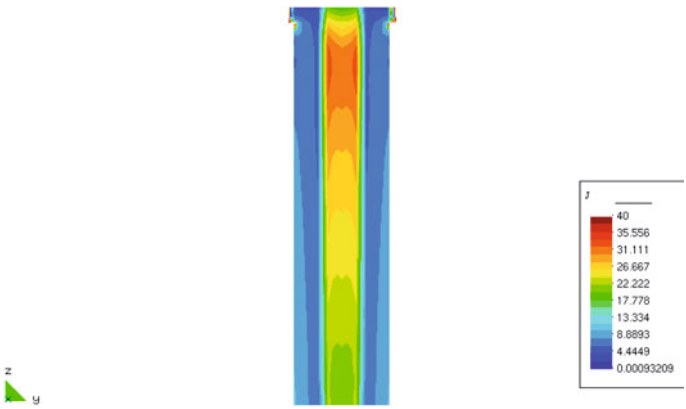

Fig. 9.9. Magnitude of the current density (A/cm^2): vertical section (courtesy of A. Bermúdez, R. Rodríguez and P. Salgado)

the external boundary: however, in this way a non-conductive air region is introduced (see Bermúdez et al. [45], Alonso Rodríguez et al. [20]).

When considering a single electrode the proximity effect is neglected: though the magnetic field generated by each electrode induces eddy currents in the other electrodes, this is not considered in the simulations. A first attempt at taking into account this effect has been carried out by Bermúdez et al. [38] for ELSA electrodes, solving numerically the electromagnetic problem on a horizontal section of the three electrodes. A drawback is that these two-dimensional models are valid only in the lower part of the electrode, where it can be assumed that the electric current is orthogonal to the considered two-dimensional section.

The more realistic modeling of the reduction furnace requires to consider a three-dimensional non-symmetric computational domain, formed by a conducting region and an insulating region. We conclude this section by presenting some numerical simulations due to Bermúdez et al. [43] for this model of the furnace, with three ELSA compound electrodes. The contact clamps and the casing are not explicitly considered in the modelization, and the Søderberg paste is assumed to be baked in the whole domain. The electric current enters the electrodes through copper bars of rectangular section. In Figures 9.10 and 9.11 we show the geometrical data of the problem.

The numerical method used for the simulations illustrated in Figures 9.12 and 9.13 is the finite element discretization analyzed in Bermúdez et al. [45], and presented in Section 5.4.2. The problem is formulated in terms of the magnetic field in the conductor and of the scalar magnetic potential in the insulator, and the finite elements used are first order edge elements in the conductor and first order nodal elements in the insulator.

Numerical results for the same problem, but formulated in terms of the electric field in the conductor and of the scalar magnetic potential in the insulator, have been also presented in Section 8.1.5.

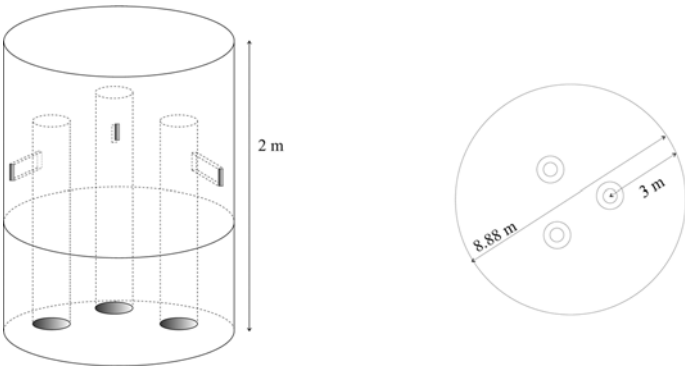

Fig. 9.10. Sketch of the model domain (courtesy of A. Bermúdez, R. Rodríguez and P. Salgado)

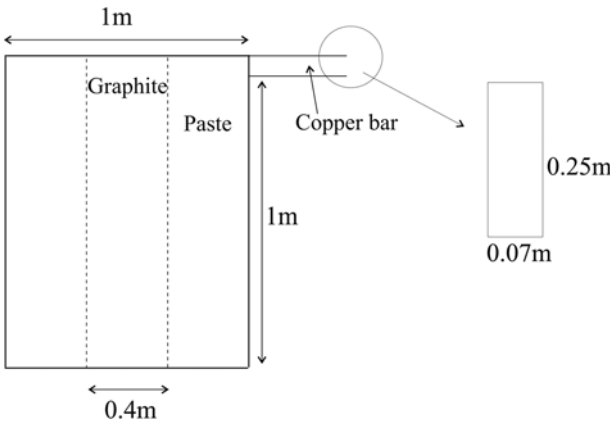

Fig. 9.11. Geometrical data corresponding to a vertical section of each electrode (courtesy of A. Bermúdez, R. Rodríguez and P. Salgado)

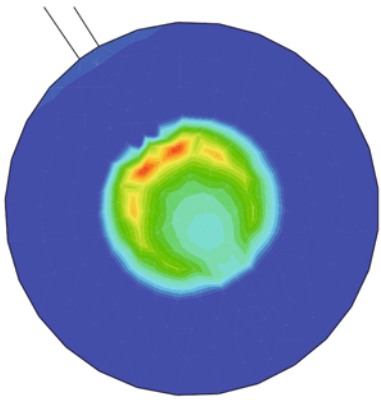

Fig. 9.12. Magnitude of the current density (A/cm^2): horizontal section (courtesy of A. Bermúdez, R. Rodríguez and P. Salgado)

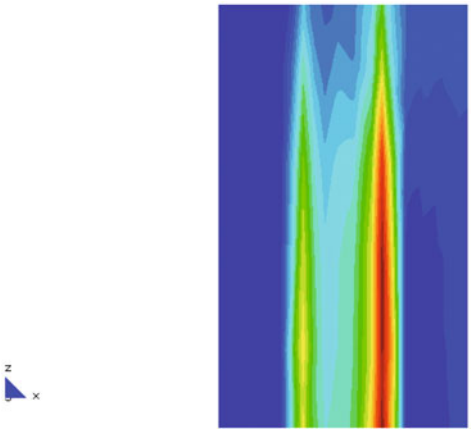

Fig. 9.13. Magnitude of the current density (A/cm^2): vertical section (courtesy of A. Bermúdez, R. Rodríguez and P. Salgado)

9.2 Bioelectromagnetism: EEG and MEG

Electroencephalography (EEG) and magnetoencephalography (MEG) are two non-invasive techniques used to localize electric activity in the brain from measurements of external electromagnetic signals. Electroencephalography measures the scalp electric potential, while magnetoencephalography measures the external magnetic flux.

The electromagnetic activity of the brain is due to the movements of ions within activated regions of the cortex sheet, the so-called impressed currents (or primary currents). In addition, Ohmic currents are generated in the surrounding medium, the so-called return currents. The measures of EEG and MEG correspond to both impressed and return currents, but the source of interest are the impressed currents, as they represent the area of neural activity associated to a sensory stimulus.

The first EEG recording in man (and the name Electroenkephalogram) is due to H. Berger in 1924. He measured electric potential differences between pairs of electrodes placed on the scalp. Nowadays these electrodes can be directly glued to the skin or fitted in an elastic cap, and tipically up to 256 electrodes are used (see in Figure 9.14 a cap with 128 electrodes).

The first magnetoencephalograms date back at the late 1960s by D. Cohen. The magnetic signal related to brain activity is extremely weak, about 10^8 times lower than the earth's geomagnetic field. Its measurement only becames possible with the SQUID (Superconducting QUantum Interface Devices) magnetometer introduced by Zimmerman [249]. This kind of instrumentation measures some component of the magnetic induction on different locations, nowadays up to 100, close but external to the head (see Figure 9.15).

For a comprehensive introduction to theory and instrumentation in MEG see Hämäläinen et al. [117]. A complete description of the models used in EEG/MEG

Fig. 9.14. The distribution of the sensors for EEG

Fig. 9.15. The distribution of the sensors for MEG (courtesy of Elekta)

source localization is provided in Baillet et al. [34] (see also Mosher et al. [182]). Let us give here a concise presentation of the topic.

Source localization is an inverse problem: knowing the value of the magnetic field or of the electric field on the surface of the head (or, possibly, external to the head, but close to its surface), the aim is to determine the position and some physical characteristics of the current density that has given rise to that value.

Since the current distribution inside a conductor cannot be retrieved uniquely from knowledge of the electromagnetic field outside the conductor, the mathematical problem does not have a unique solution if some additional conditions on the source model are not assumed (see Sarvas [220]). Two different approaches are mainly used to reconstruct the brain neural sources: equivalent dipole and distributed source models.

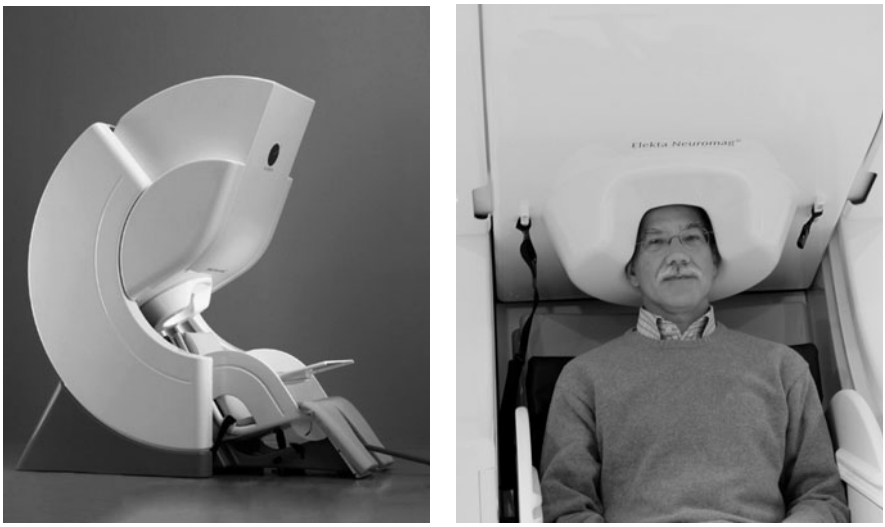

Fig. 9.16. The Elekta Neuromag MEG system (left, courtesy of Elekta) and the second author in the CIMeC Laboratory, University of Trento (right)

Moreover, see for instance Kaipio and Somersalo [142] for statistical approaches that we do not consider here.

In the dipolar model the primary current distribution is represented as a point source located at $\mathbf{x}_q$ with moment $\mathbf{q}$, namely,

$$\mathbf{J}_e(\mathbf{x}) = \mathbf{q}\,\delta(\mathbf{x} - \mathbf{x}_q)\,,$$

where $\delta(\cdot)$ is the Dirac delta distribution. The dipole is a convenient representation for a unidirectional impressed current due to the activation of a large number of pyramidal cells, that in real situations may indeed extend over several square centimeters of the cortex. More generally, it is assumed that a primary current source can be decomposed as the sum of (few) current dipoles. In the standard dipolar method the parameters of the dipoles (location, amplitude and orientation) are found using a nonlinear least-squares search.

The distributed source model (also called imaging approach) assumes that a lot of dipoles are located perpendicularly to the cortical surface. The geometry of the cortical surface can be extracted from brain magnetic resonance imaging (MRI) data. A tessellation of this surface is constructed and a current dipole is placed on each element with itsorientation normal to the surface. The inverse problem in this case turns out to be linear: only the magnitudes of the dipole moments have to be reconstructed, and not the location nor the orientation. Proceeding in this way the number of unknowns is typically greater than the number of measured data and the inverse problem is solved using regularization schemes, such as a truncated singular value decomposition of the Tikhonov regularization.

In both cases, a preliminary step for the solution of the inverse problem is an efficient resolution of the forward problem. In fact, the procedure is essentially the following: given a source $\mathbf{J}_e$, solve the forward problem, thus determining the electric and magnetic fields generated by $\mathbf{J}_e$, and then minimize in a suitable way the difference between the computed and the measured data. The current density $\mathbf{J}_e^*$ which achieves the minimum is the source we are trying to determine.

Let us focus now on the forward problem. For biological tissues, the linear constitutive equations $\mathcal{D} = \varepsilon\mathcal{E}$ and $\mathcal{B} = \boldsymbol{\mu}\mathcal{H}$ can be assumed (see Plonsey and Heppner [194]). Due to its complicated detailed structure, the human brain must be modeled as a heterogeneous anisotropic medium, with physical parameters that depend on the spatial variable and that may be tensors. The frequency spectrum for electrophysiological signals in MEG is tipically below 1000 Hz, and most studies deal with frequency between 0.1 and 100 Hz.

As far as we know, in almost all the studies concerning the neural generation of electromagnetic fields the static approximation of Maxwell equations is considered

$$\begin{aligned} &\operatorname{curl}\mathbf{H} = \mathbf{J} \\ &\operatorname{div}\mathbf{B} = 0 \\ &\operatorname{curl}\mathbf{E} = \mathbf{0}\,, \end{aligned} \tag{9.1}$$

neglecting not only the displacement current but also the electromagnetic diffusion.

From Ohm law the total current density $\mathbf{J}$ is the sum of the impressed currents plus the return currents

$$\mathbf{J} = \mathbf{J}_e + \boldsymbol{\sigma}\mathbf{E} = \mathbf{J}_e - \boldsymbol{\sigma}\operatorname{grad} V\,,$$

where V is the electric scalar potential. From the first equation in (9.1) it follows that

$$0 = \operatorname{div}\mathbf{J} = \operatorname{div}(\mathbf{J}_e - \boldsymbol{\sigma}\operatorname{grad} V)\,.$$

Hence V can be obtained by solving the Poisson equation

$$\operatorname{div}(\boldsymbol{\sigma}\operatorname{grad} V) = \operatorname{div}\mathbf{J}_e\,, \tag{9.2}$$

usually with the boundary condition $\boldsymbol{\sigma}\operatorname{grad} V \cdot \mathbf{n} = \mathbf{J}_e \cdot \mathbf{n}$, which is a consequence of the fact that outside the head the magnetic field is supposed to be curl-free (the source $\mathbf{J}_e$ is located inside the head, and the conductivity is vanishing outside the head, so that $\mathbf{J} = \mathbf{0}$).

For EEG this is the point: solving this elliptic problem gives the electric field, and the inverse problem of source localization can be dealt with.

For MEG, one has to go further. Since the magnetic permeability can be assumed to be homogeneous and equal to μ_0, the free-space permeability, $\mathbf{B}$ is given by the Biot-Savart law

$$\mathbf{B}(\mathbf{x}) = \frac{\mu_0}{4\pi}\int_{\mathbb{R}^3} \mathbf{J}(\mathbf{y}) \times \frac{\mathbf{x}-\mathbf{y}}{|\mathbf{x}-\mathbf{y}|^3}\,d\mathbf{y}\,. \tag{9.3}$$

Here the integration is indeed carried out on a bounded domain Ω, representing the head, as $\mathbf{J}$ is vanishing outside Ω. Note that this formula furnishes a direct way to

compute the magnetic induction $\mathbf{B}$, but only after we have determined the electric scalar potential V through (9.2).

However, in some cases solving the elliptic problem (9.2) can be avoided. In fact, the typical (though simplified) head model assumes that the head can be described by three (scalp, skull and brain) to five (scalp, skull, cerebrospinal fluid, gray matter and white matter) contiguous layers Ω_j, $j = 1, \ldots, n$. The different layers of the head and the air region are separated by the surfaces S_j, $j = 1, \ldots, n$, S_1 being the outermost one. Assuming that the conductivity of each layer is a scalar constant, by employing classical results of potential theory it is possible to derive a surface integral equation for $V_k := V_{|S_k}$, $k = 1, \ldots, n$,

$$\begin{aligned} &\frac{\sigma_k^- + \sigma_k^+}{2} V_k(\mathbf{x}) \\ &\quad = V_\infty(\mathbf{x}) - \frac{1}{4\pi} \sum_{j=1}^{n} (\sigma_j^- - \sigma_j^+) \int_{S_j} V_j(\mathbf{y})\, \mathbf{n}_j(\mathbf{y}) \cdot \frac{\mathbf{x}-\mathbf{y}}{|\mathbf{x}-\mathbf{y}|^3}\, dS_y \end{aligned} \tag{9.4}$$

(see Sarvas [220]), where

$$V_\infty(\mathbf{x}) := \frac{1}{4\pi} \int_\Omega \mathbf{J}_e(\mathbf{y}) \cdot \frac{\mathbf{x}-\mathbf{y}}{|\mathbf{x}-\mathbf{y}|^3}\, d\mathbf{y}\,,$$

$\mathbf{n}_j$ is the unit outward normal vector to S_j, σ_j^- is the inside conductivity and σ_j^+ is the outside conductivity, with $\sigma_1^+ = 0$ and, clearly, $\sigma_j^- = \sigma_{j+1}^+$, $j = 1, \ldots, n-1$. Note that, in the particular case of a current dipole, one has

$$V_\infty(\mathbf{x}) = \frac{1}{4\pi}\, \mathbf{q} \cdot \frac{\mathbf{x}-\mathbf{x}_q}{|\mathbf{x}-\mathbf{x}_q|^3}\,.$$

For constant conductivities integration by parts in (9.3) shows that also the Biot–Savart law can be written as a sum of surface integrals on the interfaces between layers, obtaining the formula due to Geselowitz [109]

$$\mathbf{B}(\mathbf{x}) = \mathbf{B}_\infty(\mathbf{x}) - \frac{\mu_0}{4\pi} \sum_{j=1}^{n} (\sigma_j^- - \sigma_j^+) \int_{S_j} V_j(\mathbf{y})\, \mathbf{n}_j(\mathbf{y}) \times \frac{\mathbf{x}-\mathbf{y}}{|\mathbf{x}-\mathbf{y}|^3}\, dS_y\,, \tag{9.5}$$

where the vector field

$$\mathbf{B}_\infty(\mathbf{x}) := \frac{\mu_0}{4\pi} \int_\Omega \mathbf{J}_e(\mathbf{y}) \times \frac{\mathbf{x}-\mathbf{y}}{|\mathbf{x}-\mathbf{y}|^3}\, d\mathbf{y}$$

is called the primary field. In the case of a current dipole it becomes

$$\mathbf{B}_\infty(\mathbf{x}) = \frac{\mu_0}{4\pi}\, \mathbf{q} \times \frac{\mathbf{x}-\mathbf{x}_q}{|\mathbf{x}-\mathbf{x}_q|^3}\,.$$

At this stage, for MEG the main point turns out to be the determination of the functions V_j on the surfaces S_j, which furnish the magnetic induction $\mathbf{B}$ via the explicit formula

(9.5). Hence a boundary element approach can be introduced, with the aim of finding a solution to the discrete approximation of (9.4), then inserting the obtained results in (9.5).

In some particular cases one can even avoid solving (9.4). Indeed, a simplified model assumes that the head consists of a set of nested concentric spheres, each layer with a scalar constant conductivity. In the special case of a current dipole and of a MEG system that measures only the radial component of the magnetic induction $\mathbf{B}$, the contribution of the return currents vanishes, as for $\mathbf{y} \in S_j$ and $\mathbf{x} \neq \mathbf{y}$ one has

$$\begin{aligned}&\left(\mathbf{n}_j(\mathbf{y}) \times \tfrac{\mathbf{x}-\mathbf{y}}{|\mathbf{x}-\mathbf{y}|^3}\right) \cdot \tfrac{\mathbf{x}}{|\mathbf{x}|} \\ &\quad = \left(\tfrac{\mathbf{y}}{|\mathbf{y}|} \times \tfrac{\mathbf{x}}{|\mathbf{x}-\mathbf{y}|^3}\right) \cdot \tfrac{\mathbf{x}}{|\mathbf{x}|} - \left(\tfrac{\mathbf{y}}{|\mathbf{y}|} \times \tfrac{\mathbf{y}}{|\mathbf{x}-\mathbf{y}|^3}\right) \cdot \tfrac{\mathbf{x}}{|\mathbf{x}|} = 0\,.\end{aligned}$$

Therefore, the radial component of $\mathbf{B}(\mathbf{x})$ reduces to

$$B_r(\mathbf{x}) = \frac{\mathbf{x}}{|\mathbf{x}|} \cdot \mathbf{B}(\mathbf{x}) = \frac{\mathbf{x}}{|\mathbf{x}|} \cdot \mathbf{B}_\infty(\mathbf{x}) = \frac{\mu_0}{4\pi} \frac{\mathbf{x} \times \mathbf{x}_q}{|\mathbf{x}||\mathbf{x} - \mathbf{x}_q|^3} \cdot \mathbf{q} \tag{9.6}$$

(note the linear dependence of B_r on the moment $\mathbf{q}$ and the nonlinear dependence on the position $\mathbf{x}_q$). Hence, the radial component of $\mathbf{B}$ turns out to be independent of the potential V, and in this case the solution of the inverse MEG problem does not require the previous computation of V, and simply uses the explicit formula (9.6).

These spherical models work reasonably well and are routinely used in most applications of EEG and MEG source localization. However, it seems clear that, in order to improve the source reconstruction, more accurate solutions to the forward problem are needed, and a more realistic model must be considered. Anatomical information can be obtained from brain magnetic resonance imaging or X-ray computed tomography imaging (see, for instance, Khan et al. [151]). From these images it is possible to construct a realistic head model (see, e.g., Van Uiter et al. [239], Kybic et al. [162], Wolters et al. [245]) and extract precise informations about surface boundaries for scalp, skull and brain. On the other hand, recent studies of Marin et al. [172], Wolters et al. [244], and Haueisen et al. [118] show that the anisotropy of the conductivity in the skull and brain must be taken into account and in particular the conductivity cannot be assumed to be piecewise-constant. From a numerical point of view this means that one has to go back to the numerical solution of (9.2), and this can be done by using a finite element scheme.

However, a modelization through the elliptic equation (9.2) is not completely satisfactory. In fact, as already remarked, the physiological frequency involved in the problem ranges between 0.1 and 100 Hz, and in general cannot be assumed to vanish. Therefore the static model (9.1) has to be replaced by the eddy current model. To the best of our knowledge, the latter has not been used yet for brain activity reconstruction from MEG data, but this could be an important direction for further researches.

In this respect, since it is necessary to reduce as far as possible the computational cost of the forward solver, the approach presented in Sections 7.1–7.5 could be a useful tool.

Remark 9.1. The necessity of taking into account a non-vanishing frequency has been underlined by He and Romanov [122], Ammari et al. [22], who use the full Maxwell

system as forward problem. They consider the inverse source problem that arises in determining the location of an epileptic focus, i.e., the localization of a single dipole in a homogeneous or even heterogeneous medium. Unlike many inverse methods, the proposed algorithm is non-iterative. Following Ammari et al. [22], in this case the considered forward problem is the time-harmonic full Maxwell system in $\mathbb{R}^3$

$$\begin{aligned} &\operatorname{curl}\mathbf{H} - i\omega\boldsymbol{\varepsilon}\mathbf{E} = \boldsymbol{\sigma}\mathbf{E} + \mathbf{q}\,\delta(\mathbf{x}-\mathbf{x}_q) \\ &\operatorname{curl}\mathbf{E} + i\omega\boldsymbol{\mu}\mathbf{H} = \mathbf{0}\,, \end{aligned} \tag{9.7}$$

with the Silver–Müller radiation condition

$$\lim_{|\mathbf{x}|\to+\infty} |\mathbf{x}| \left(\sqrt{\mu_0}\,\mathbf{H} \times \frac{\mathbf{x}}{|\mathbf{x}|} - \sqrt{\varepsilon_0}\,\mathbf{E} \right) = \mathbf{0}\,,$$

ε_0 being the free-space electric permittivity.

As usual, let Ω_C denote the conductor (the human head). If φ is a scalar harmonic function in Ω_C and $\mathbf{u}$ is a solution to

$$\operatorname{curl}(\mu_0^{-1} \operatorname{curl}\mathbf{u}) = i\sigma \operatorname{grad}\varphi\,,$$

then it can be proved that

$$\mathbf{q}\cdot\operatorname{grad}\varphi(\mathbf{x}_q) = \int_{\partial\Omega_C} \mathbf{H}\times\mathbf{n}\cdot\operatorname{grad}\varphi + i\int_{\partial\Omega_C} \mu_0^{-1}\operatorname{curl}\mathbf{u}\cdot\mathbf{E}\times\mathbf{n} + O(\omega)\,.$$

Choosing in this formula six particular harmonic functions ($\varphi_k = x_k$ for $k = 1,2,3$ and $\varphi_k = e^{i\boldsymbol{\xi}_{k-3}\cdot\mathbf{x}}$ for $k = 4,5,6$, where $\boldsymbol{\xi}_j \in \mathbb{C}^3$, $j = 1,2,3$, are such that $\sum_{i=1}^3 \xi_{j,i}^2 = 0$), the six components of $\mathbf{q}$ and $\mathbf{x}_q$ can be approximated. It is worth noting that this reconstruction is carried out without a priori knowledge of the angular frequency ω. □

Remark 9.2. A related forward problem, where the eddy current system or else the full Maxwell equations have been adopted, is the numerical simulation of transcranial magnetic stimulation (TMS): see, e.g., Ueno et al. [237], Sekino et al. [225]. This is a non-invasive method for stimulating neurons in the brain, and it is widely used in neuroscience, in order to study the functional organization of human brain, and in the diagnosis and the treatement of neurological diseases. A transcranial magnetic stimulation system consists in a coil placed on the scalp, that produces a time-harmonic magnetic field which induces eddy currents in the brain. The operating frequency ranges from 1 to 4 kHz. It is also possible to use more than one coil to stimulate different parts of the brain simultaneously: this is the so-called multichannel transcranial magnetic stimulation, that has recently attracted particular interest (see Lu et al. [170] and references therein).

Accurate numerical simulations of the induced fields inside the brain are necessary for optimizing the design of the coils that have to generate the desired stimulation. □

9.3 Magnetic levitation

Due to the relatively low frequencies involved, magnetic levitation problems are an interesting field of application for eddy current models: in fact, "the magnetic energy storage is dominant (as compared to energy stored in the electric field) and wave phenomena are small enough to be ignored" (Thompson [234]; see also, e.g., Kriezis et al. [157]).

Let us start this section with a brief presentation of problem 28 of the TEAM workshop, a simple electrodynamic levitation problem which can serve as a model problem for more complex computations in moving domains. It is an axisymmetric transient problem with electromechanical coupling (see Karl et al. [148] and Kurz et al. [161]). The device is described as follows: a cylindrical aluminium plate is located above two cylindrical coils, formed by electric wires, all the parts with the same axis (see Figures 9.17 and 9.18). At the initial instant the plate is above the coils at a certain distance, then an applied current density is imposed. Both coils are connected in series, with different sense of winding.

Fig. 9.17. The geometry in problem 28 of the TEAM workshop

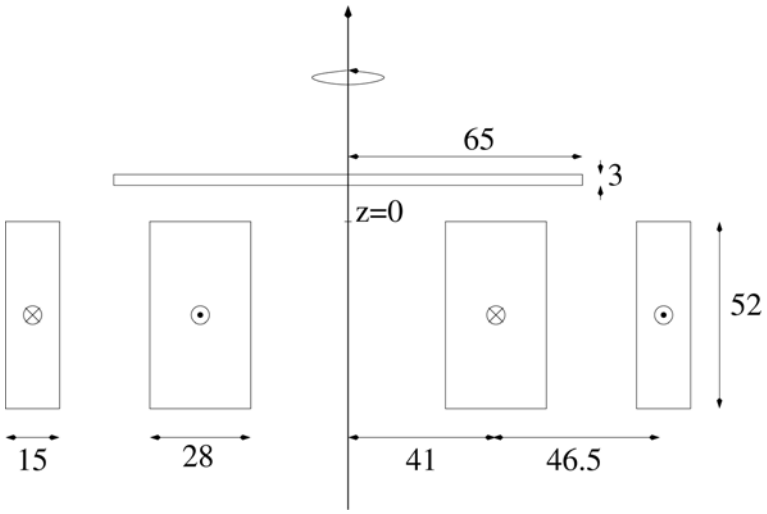

Fig. 9.18. The dimensions in problem 28 of the TEAM workshop

Due to the induced eddy currents, a repulsive Lorentz force

$$\mathbf{F}_L(\mathbf{u},\mathbf{E},\mathbf{B}) := \int_{\Omega_C} [\boldsymbol{\sigma}(\mathbf{E}+\mathbf{u}\times\mathbf{B})]\times\mathbf{B}$$

acts on the plate Ω_C, which reaches, after a transient time, a stationary levitation height. Here $\mathbf{u}$ denotes the velocity of the plate, which depends on mechanical as well as electromagnetic forces, in particular on $\mathbf{B}$ and $\mathbf{E}$.

From the mathematical point of view, the problem is described by the time-dependent eddy current equations

$$\begin{cases} \operatorname{curl}\mathbf{H}-\boldsymbol{\sigma}\mathbf{E}=\mathbf{J}_e+\boldsymbol{\sigma}(\mathbf{u}\times\mathbf{B}) & \text{in } \Omega \\ \operatorname{curl}\mathbf{E}+\frac{\partial\mathbf{B}}{\partial t}=\mathbf{0} & \text{in } \Omega \\ \operatorname{div}(\boldsymbol{\varepsilon}_I\mathbf{E}_I)=0 & \text{in } \Omega_I\ , \end{cases} \tag{9.8}$$

where Ω is a "box" containing the plate and the support of the coils, and $\mathbf{J}_e$ is supported only in the coils.

The constitutive relation between $\mathbf{B}$ and $\mathbf{H}$ in general is given by $\mathbf{B}=\boldsymbol{\mu}\mathbf{H}+\mathbf{M}$, where $\mathbf{M}$ is the magnetization; however, as always done in this book, here below we assume that $\mathbf{M}=\mathbf{0}$.

Employing an implicit time-discretization scheme and computing the nonlinear term $\mathbf{u}\times\mathbf{B}$ at the previous time level leads at each time step to the solution of

$$\begin{cases} \operatorname{curl}\mathbf{H}^{n+1}-\boldsymbol{\sigma}\mathbf{E}^{n+1}=\mathbf{J}_e^{n+1}+\boldsymbol{\sigma}(\mathbf{u}^n\times\mathbf{B}^n) & \text{in } \Omega \\ \operatorname{curl}\mathbf{E}^{n+1}+\mathbf{B}^{n+1}/\Delta t=\mathbf{B}^n/\Delta t & \text{in } \Omega \\ \operatorname{div}(\boldsymbol{\varepsilon}_I\mathbf{E}_I^{n+1})=0 & \text{in } \Omega_I\ . \end{cases} \tag{9.9}$$

Then at the time step $n+1$ the velocity $\mathbf{u}$ and the position $\mathbf{r}$ of the center of gravity of the plate are obtained by setting

$$\mathbf{u}^{n+1}=\mathbf{u}^n+\mathbf{g}+m^{-1}\Delta t\,\mathbf{F}_L(\mathbf{u}^n,\mathbf{E}^{n+1},\mathbf{B}^{n+1}),$$

and

$$\mathbf{r}^{n+1}=\mathbf{r}^n+\Delta t\,\mathbf{u}^{n+1}\,,$$

where $\mathbf{g}$ is the acceleration of gravity, m the mass of the plate and $\mathbf{F}_L$ the Lorentz force.

Most of the results that we have presented for time-harmonic eddy current problems can be adapted to the system of equations (9.9). For instance, Kurz et al. [161] have computed the levitation height by using a FEM–BEM approach for the $(\mathbf{A}_C,V_C)-\mathbf{A}_I$ vector potential formulation. Moreover, Rapetti [201] has used an approach based on the vector potential $\mathbf{A}$ and on an overlapping mortar element technique for taking into account the movement of the plate.

In particular, in the TEAM workshop problem 28 the data of the problem are as follows: the mass of the plate is $m=0.107$ kg, the initial distance of the plate from the coils is 3.8 mm, the applied current density is given by $\mathbf{J}_e(t)=(-1)^k J_k I^0\sin(\omega t)\mathbf{e}_\phi$, where $\mathbf{e}_\phi$ is the (counterclockwise) azymuthal unit vector in the cylindrical system,

$k = 1$ refers to the outer coil and $k = 2$ to the inner coil, $I^0 = 20$ A, $\omega = 2\pi \times 50$ rad/s, $J_1 = N_1/S_1$ and $J_2 = N_2/S_2$, where $N_1 = 576$ and $N_2 = 960$ are the number of turns of the electric wires in the coils, and S_1 and S_2 are the cross sections. Finally, the conductivity and the permeability are given by $\sigma = 3.4 \times 10^7$ S/m, $\mu = 4\pi \times 10^{-7}$ H/m.

The results obtained by Kurz et al. [161] and Rapetti [201] are in very good agreement with the experimental data: after a transient time of about 1.6 ms, a stationary levitation height of about 11.3 mm is reached.

TEAM workshop problem 28 is clearly a very simplified model for realistic phenomena based on magnetic levitation. In order to give a more detailed description of the effective technological problems related to this topic, below we briefly outline a presentation of magnetic levitation trains.

Since the 1960s some industrial companies attempted to design a train without wheels, suspended over a specialized track by magnetic levitation and with a propulsion system based on magnetic forces (for more details about these early projects, see, e.g., the review papers by Thornton [235], Yamamura [246], Rogg [213], Powell and Danby [195]).

Two related but different techniques have been mainly used to reach this goal: electrodynamic levitation with superconducting magnets and electromagnetic levitation with normal conductive magnets (for an up-to-date presentation of these technologies, see, e.g., Cassat and Jufer [75], Lee et al. [164], Yan [247]).

In electrodynamic levitation the train is lifted and guided by means of repulsive forces between superconducting coils placed on the vehicle and coils inserted in the guideway (see Figure 9.19). The repulsive forces are produced only when the magnets are moving, hence the train does not levitate at low speed and it still needs wheels for "take-off and landing". The air gap (the distance between the vehicle and the ground) can be larger that 10 cm, and the system turns out to be magnetically stable: if the levitation height becomes lower than the equilibrium position, the magnetic repulsion

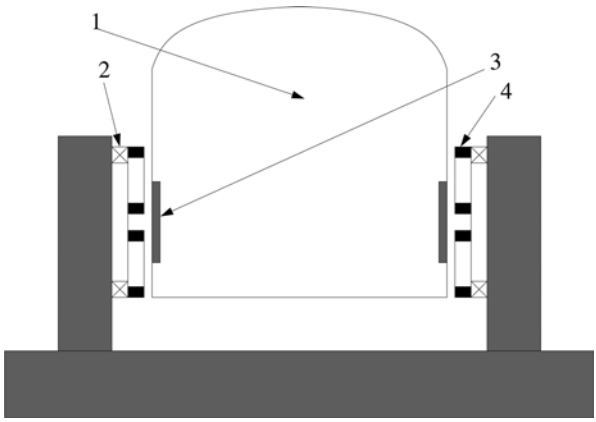

Fig. 9.19. Scheme of the electrodynamic levitation system: 1 vehicle, 2 propulsion windings, 3 superconducting magnets, 4 levitation and guidance windings

force increases, restoring equilibrium; if the levitation height turns out to be too large, then gravity prevails and the air gap is reduced. For this stability property, this system is the most indicated for high speeds and for use in regions that can be subjected to strong earthquakes. The electrodynamic levitation system, originally proposed by Danby and Powell [92], has been adopted by Japanese National Railways, that since the 1970s have produced the series of MLU trains and more recently the last prototype MLX, that in 2003 obtained the train speed record of 581 km/h.

By contrast, electromagnetic levitation makes use of attracting forces between normal conducting electromagnets situated on board and an iron-core armature winding on the rail. The attracting forces produces an inherently unstable levitation system, and the air gap, which is about 1 cm and is nearly velocity-independent, has to be controlled via a high-precision device. Sensors measure the air gap and accelerometers measure the acceleration of the magnets, and information about both of these are passed to the control system. Levitation and guidance can be either integrated in a single system (see Figure 9.20), or else separated (see Figure 9.21). The first choice has been adopted for the Japanese HSST train, operating in public service since 2005 in Nagoya (short distance and medium speed), the second one for the German Transrapid train, operating since 2004 in Shanghai (long distance and high speed).

Concerning propulsion, in both levitation systems the power to the coils at the guideway is supplied by a linear synchronous motor, whose structure is simpler than that of a standard rotating electric motor, not requiring the use of mechanical coupling: plainly-speaking, it is like a conventional rotating motor in which stator, rotor and windings have been unrolled and stretched along the guideway. The working principle is the same: an alternating current inside the motor windings on the guideway generates a space–time depending magnetic field in the air gap, and it induces an electromotive force in the secondary part, a conducting sheet with (standard or superconducting)

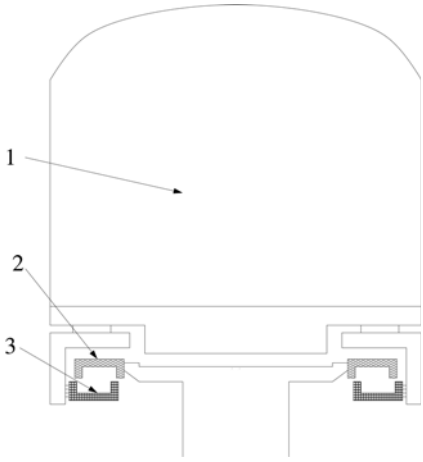

Fig. 9.20. Scheme of the electromagnetic levitation system (levitation and guidance integrated): 1 vehicle, 2 iron-core rail windings, 3 levitation and guidance magnets

magnets placed on the vehicle. This electromotive force generates the eddy currents, whose interaction with the flux in the air gap produces the thrust force. The speed is regulated by varying the frequency of the alternating current, and, if the direction of the traveling field is reversed, the motor becomes a generator and the the train is braked, without contact. The advantage given by a linear motor is that, in the case of a (more or less) rectilinear motion, its efficiency is higher than that of a rotating motor, because of the minor amount of vibration and noise.

Also guidance is based on magnetic forces. In the MLX prototype, the levitation coils on the sideways are connected in such a way that, if a train is closer to one side, then induced currents are produced and this generates a guiding force (in other words, the coils work as a guide system, based on a repulsive force). For the Transrapid train, electromagnets are placed on both sides of the vehicle, and reaction rails on the guideway interact with them maintaining the train suitably centered on the track.

Summing up, the magnetic levitation train is a technological problem of low-frequency electromagnetism coupled with dynamics. To our knowledge, a complete modeling of the whole process has not been performed, due to its high complexity. However, some of its parts have been considered in detail and analyzed by means of the finite element method, though mainly for simplified mathematical models derived from the eddy current equations: as examples we recall the calculation of the magnetic field around the HSST train magnet (see Aoki [28]) or that of induced currents and forces for an hybrid levitation magnet (see Albertz et al. [4]), the investigation of the stability of repulsive forces (see He et al. [121]), the analysis of the heating problem arising in superconducting magnets (see Saito et al. [216]), the design of high temperature superconducting coils (see Jenkins et al. [139]). Finally, the analysis of the MLX train levitation system and some of its variants has been investigated only by means of the dynamic circuit theory (see He et al. [120], Davey [96]), and would give more precise results if the analysis relied on the complete eddy current model.

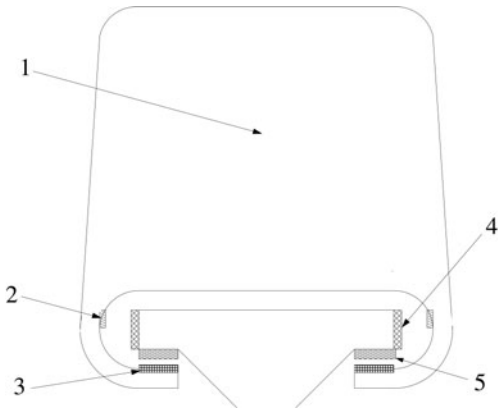

Fig. 9.21. Scheme of the electromagnetic levitation system (levitation and guidance separated): 1 vehicle, 2 guidance magnets, 3 levitation and propulsion magnets, 4 rail guidance windings, 5 iron-core rail windings

Fig. 9.22. The Transrapid magnetic levitation train in Shanghai (left) and the first author before take-off (right)

9.4 Power transformers

As it is well-known, power transformers are used to produce an alternating current with low intensity and high voltage starting from an alternating current with high intensity and low voltage, and viceversa.

In its most common form a transformer is constituted by two windings, wrapped around an iron core. A time-dependent current through the primary winding generates a time-varying magnetic field in the core, and by mutual induction this field induces a voltage in the secondary winding.

The ratio between the voltage in the secondary winding and the voltage in the primary winding is proportional to the ratio between their respective winding numbers. Therefore, tweaking on the number of turns makes it possible to tune the electromotive force at the exit of a transformer, hence to reduce the resistive loss in the conducting wires employed for the transmission of electric power from the power plant to the user.

In 1831 M. Faraday was the first to discover the electromagnetic induction between coils, but the first transformer for commercial use, based on an alternating current for creating the flux variations necessary for induction, was designed by W. Stanley in 1886 (see Figure 9.23).

Nowadays, transformers are in general polyphase; the most common used in electric power distributions are three-phase transformers (see Figures 9.24 and 9.25).

Looking in more detail, their structure can be rather complicated, as they include the coils and the core, an oil tank for refrigeration and insulation, pressing and clamping plates around the coils, shields at the walls of the tank.

With the increase of the power, stray losses become more and more important, lowering the efficiency of transformers and producing significative local overheating in the metallic components: by Joule effect the current in the windings generates a resistive heating, eddy currents are responsible of the increasing of the heat in the core, and the rise of the temperature also occurs in plates and shields. The reduction of these unintended effects, which influences the reliability and decreases the operating life of transformers, is one of the most important points for optimal design.

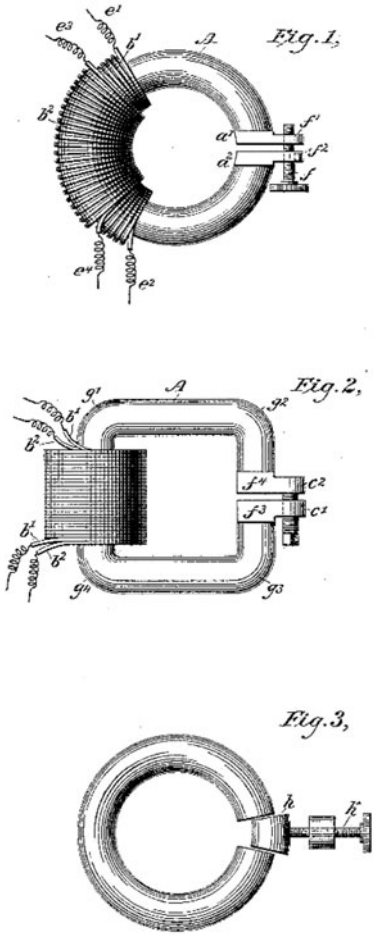

Fig. 9.23. The Stanley transformer (1886, U.S. Patent and Trademark Office)

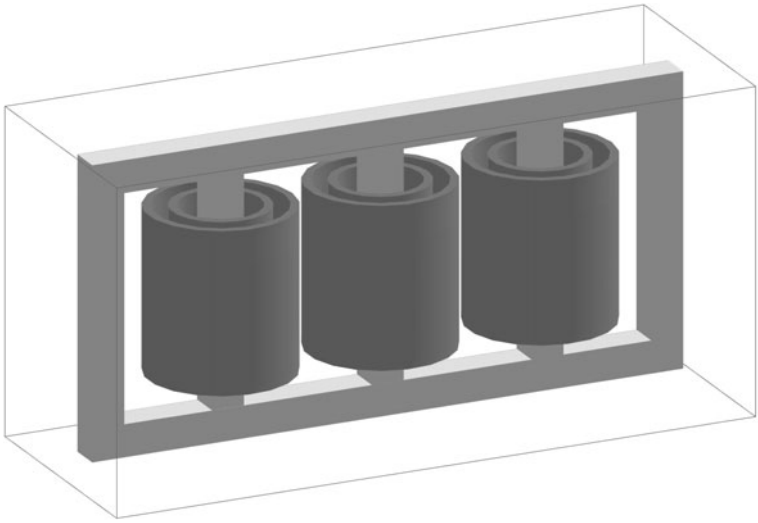

Fig. 9.24. A three-phase, five-leg transformer

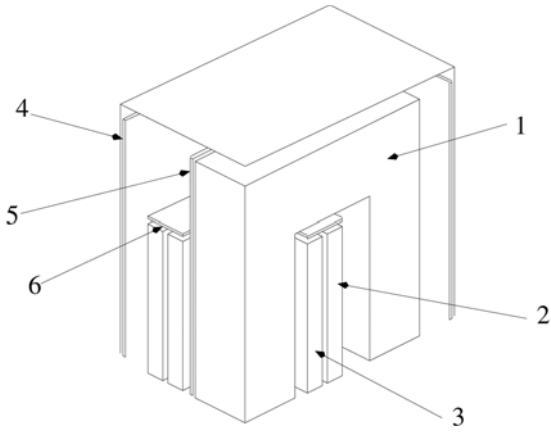

Fig. 9.25. A detail of a transformer: 1 iron core, 2 high winding, 3 low winding, 4 shielding, 5 clamping plate, 6 pressing plate

A thorough modeling of a power transformer based on the eddy current equations, possibly coupled with the heat equation, has been proposed by many authors.

Chen et al. [80] have considered the finite element approximation of a three-phase, five-leg transformer, using an approach based on a suitably modified $\mathbf{T}_C - \psi$ method, preferred to others since the current potential $\mathbf{T}_C$ only appears in the conductor, a rather small region in power transformers. Considering, for the sake of definiteness, the

magnetic boundary value problem $\mathbf{H} \times \mathbf{n} = \mathbf{0}$ on $\partial\Omega$, the magnetic field is represented as

$$\mathbf{H} = \begin{cases} \operatorname{grad} \psi_I + \mathbf{K}_I & \text{in } \Omega_I \\ \mathbf{T}_C + \operatorname{grad} \psi_C + \mathbf{K}_C & \text{in } \Omega_C \,, \end{cases}$$

where $\mathbf{K}_I \in \mathcal{H}_{\mu_I}(\partial\Omega, \Gamma; \Omega_I)$, $\mathbf{K}_C \in H(\text{curl}; \Omega_C)$ and satisfies $\mathbf{K}_C \times \mathbf{n}_C + \mathbf{K}_I \times \mathbf{n}_I = \mathbf{0}$ on Γ, and $\psi_I = \psi_C$ and $\mathbf{T}_C \times \mathbf{n}_C = \mathbf{0}$ on Γ. Note that the terms $\mathbf{K}_I$ and $\mathbf{K}_C$ are related to the topology of the domain, and cannot be discarded if the conductor Ω_C is not simply-connected.

The windings are modeled as a conducting region, and the conductivity σ assumes two different constant values in the windings and in the core. Therefore, Ω_C has several connected components, and at least one of them (the core) is not simply-connected.

The magnetic permeability μ is assumed to be a positive constant in the whole transformer, and, moreover, a Lorenz-like gauge

$$\operatorname{div} \mathbf{T}_C = -i\omega\sigma\mu_C\psi_C \qquad \text{in } \Omega_C$$

is used, in order to resort to the problem

$$-\Delta\mathbf{T}_C + i\omega\mu_C\sigma\mathbf{T}_C = \operatorname{curl} \mathbf{J}_{e,C} - \operatorname{curl}\operatorname{curl} \mathbf{K}_C - i\omega\mu_C\sigma\mathbf{K}_C \,.$$

Chen et al. [80] have computed the distribution of the eddy current density on the metallic parts of the tank, with the aim of determining the best design for their shape. In particular, they have shown that the maximum reduction of stray losses is obtained with the use of vertical magnetic shunts instead of aluminium screens.

The same approach has been proposed by Tang et al. [230] for computing the magnetic field on pressing plates, yoke-clamps and the tank wall when both windings and heavy current leads are taken into account, with the aim of optimizing the shape and dimension of a copper shield employed for minimizing overheating in the wall.

The $\mathbf{T}_C - \psi$ method has been also used by Preis et al. [196], for computing the electromagnetic field and the temperature rise in bushing adapters carrying eddy currents due to high-current low-voltage leads. In that paper the coupling with the heat equation has been taken into account, considering the Joule effect due to the eddy currents and assuming that the conductivity σ is a positive scalar function depending in a nonlinear way on the temperature. An iterative coupling strategy has been proposed, with the choice of recalculating the magnetic field in the conductor only, in order to avoid the heavy computations related to the solution of the complete electromagnetic problem.

However, as explained in Chapter 6, the $\mathbf{T}_C - \psi$ approach has various flaws, as it does not include the Faraday equation on the "cutting" surfaces, that are indeed present in multi-phase power transformers, as the conductor is not simply-connected. Moreover, the use of nodal elements, which is natural for this formulation, is not the best choice for the approximation of a problem where the conductor is a polyhedral nonconvex domain, as the convergence of the approximate solutions could fail. Therefore, a better modeling of power transformers could be achieved by resorting to one of the formulations that are more suitable for problems with complex topology (for instance, those presented in Chapters 4 and 5).

Tang et al. [231] and Ho et al. [131], employing the $(\mathbf{A}, V_C) - \mathbf{A}_I$ formulation with Coulomb gauge, has considered the numerical simulation of transient eddy current fields in power transformers connected to voltage source through electric circuits. The windings are modeled as coils included in the insulator Ω_I, and there the current density is written in the form $\mathbf{J}_{e,I}(t) = \frac{N}{S}\,\mathbb{I}(t)\,\mathbf{t}$, where $\mathbf{t}$ is the unit coil direction vector, tangential to the windings, N is the number of turns in the coil, S is its cross section and $\mathbb{I}(t)$ is the unknown current intensity. Outside the windings and in the conductor the applied current density is assumed to vanish.

Since the total induced electromotive force in windings can be expressed in term of the vector magnetic potential as follows

$$\text{emf} = \frac{N}{S}\frac{d}{dt}\int_{\Omega_w} \mathbf{A}\cdot\mathbf{t}\,,$$

where Ω_w is the space filled by windings, the problem is closed by adding a suitable equation, representing a circuit model of power transformers. Summing up, for the magnetic boundary value problem $\mathbf{H}\times\mathbf{n} = \mathbf{0}$ on $\partial\Omega$ and a domain Ω of simple shape, the global problem reads

$$\begin{cases} \operatorname{curl}(\boldsymbol{\mu}^{-1}\operatorname{curl}\mathbf{A}) - \mu_*^{-1}\operatorname{grad}\operatorname{div}\mathbf{A} \\ \qquad +\boldsymbol{\sigma}\frac{\partial}{\partial t}\mathbf{A} + \boldsymbol{\sigma}\operatorname{grad}V_C - \frac{N}{S}\,\mathbb{I}\,\mathbf{t} = \mathbf{0} & \text{in } \Omega\times(0,T) \\ \operatorname{div}(\boldsymbol{\sigma}\frac{\partial}{\partial t}\mathbf{A}_C + \boldsymbol{\sigma}\operatorname{grad}V_C) = 0 & \text{in } \Omega_C\times(0,T) \\ (\boldsymbol{\sigma}\frac{\partial}{\partial t}\mathbf{A}_C + \boldsymbol{\sigma}\operatorname{grad}V_C)\cdot\mathbf{n}_C = 0 & \text{on } \Gamma\times(0,T) \\ \mathbf{A}\cdot\mathbf{n} = 0 & \text{on } \partial\Omega\times(0,T) \\ (\boldsymbol{\mu}^{-1}\operatorname{curl}\mathbf{A})\times\mathbf{n} = \mathbf{0} & \text{on } \partial\Omega\times(0,T) \\ \frac{N}{S}\frac{d}{dt}\int_{\Omega_w}\mathbf{A}\cdot\mathbf{t} + L\,\frac{d\mathbb{I}}{dt} + R\,\mathbb{I} = V & \text{on } (0,T), \end{cases} \tag{9.10}$$

plus suitable initial conditions for $\mathbf{A}$ and $\mathbb{I}$, where L is the inductance, R the resistance, and V the voltage source of the circuit modeling the transformer. Here, the current density $\frac{N}{S}\,\mathbb{I}\,\mathbf{t}$ is intended to vanish outside the windings Ω_w.

In particular, Tang et al. [231] and Ho et al. [131] have computed the transient performance of a single-phase, three-leg power transformer, focusing in particular on the magnetic flux density on the surface of the iron core and in the windings. For a three-phase, five-leg transformer they have determined the distribution of torsional forces acting on the coils, in order to control their robustness and stability, as well as the eddy current losses in the clamping plates, checking in this way the efficiency of a magnetic by-pass plate designed for reducing overheating.

Alternative approaches to the simulation of power transformers coupled with circuits are those described in Chapter 8. In these cases, the windings are modeled as conductors, each one with two electric ports, where the voltage drop can be assigned. The topology of the insulator Ω_I becomes more complex, but the total number of degrees of freedom in formulation (8.15) is much less than that in (9.10), therefore its numerical accuracy and efficiency should be better.

9.5 Defect detection

In this section we present non-destructive evaluation (NDE) techniques based on electromagnetic methods. The aim of these techniques is to detect and characterize defects in conducting materials without causing damage.

In eddy current non-destructive testing, a coil supplied with alternating current is placed near the conductive object being inspected. Thus eddy currents are induced and generate a secondary magnetic field. Flaws are detected by monitoring changes in this magnetic field. The measured quantity is usually the impedance of the exciting coil or of a receipt coil. One can distinguish between absolute probes, where the same coil is source and receiver, and differential probes with source coils and receptive coils. This kind of techniques is widely employed in aerospace, transportation energy, nuclear and other industries. It is used, for instance, for the in-service inspection of steam generator tubes in power plants, or for the verification of aging aircraft structures. For instance, problem 27 of the TEAM workshop concerns the detection of deep flaws in a riveted assembly of aluminum sheets with a filler between the sheets, held together by titanium fasteners (see Figure 9.26). This is an example of the kind of structures that are subjected to control in aeronautical industry.

Numerical simulations are needed for the design of the probe coil and for the qualification of monitoring device. In order to develop more reliable instruments it is important to clarify the correlation between the flaws and the changes in the generated eddy currents, and numerical simulations can be used in place of more expensive experiments. From the numerical point of view a great effort has been made in the last years to obtain efficient computational schemes to simulate probe-defect interactions: see, for instance, the pioneering works of Lord [169] and Ida and Lord [136], Rasolonjanahary et al. [204], Badics et al. [33], Sabariego and Dular [214], [215], Henneron

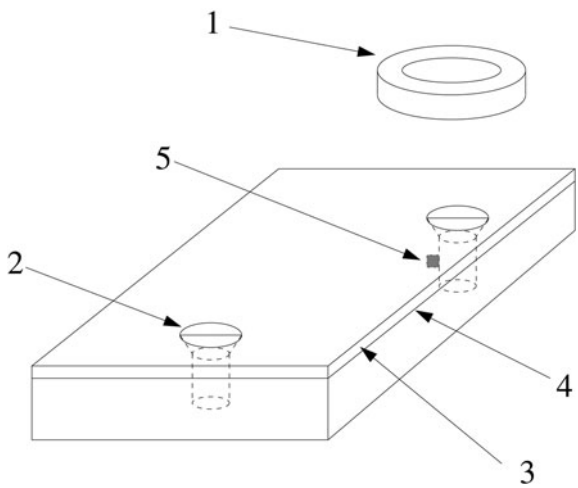

Fig. 9.26. A typical screwed assembled structure that needs to be to controlled (from problem 27 of the TEAM workshop): 1 sensor, 2 rivets, 3 sheets, 4 filler, 5 flaw to detect

et al. [125], Krebs et al. [156]; see also the review by Auld and Moulder [32] and the references therein.

Let us consider a computational domain Ω that contains the conductor Ω_C to be inspected. The electromagnetic fields generated in the case of no-flaw can be assumed to be known; in particular, they satisfy the eddy current approximation of Maxwell equations

$$\begin{array}{ll} \operatorname{curl} \mathbf{H}^u - \boldsymbol{\sigma}^u \mathbf{E}^u = \mathbf{J}_e & \text{in } \Omega \\ \operatorname{curl} \mathbf{E}^u + i\omega \boldsymbol{\mu}^u \mathbf{H}^u = \mathbf{0} & \text{in } \Omega\,, \end{array} \tag{9.11}$$

where the superscript u denotes unflawed quantities.

The impedance of the unflawed configuration is given by

$$Z^u = \frac{1}{|I^0|^2} \left(\int_{\Omega_C} \boldsymbol{\sigma}^u \mathbf{E}^u \cdot \overline{\mathbf{E}^u} + i\omega \int_{\Omega} \boldsymbol{\mu}^u \mathbf{H}^u \cdot \overline{\mathbf{H}^u} \right), \tag{9.12}$$

where I^0 is the applied current intensity (see, e.g., Jackson [137], p. 266).

Let us now assume that a flaw Ω_f (typically, a non-conducting region) is present in Ω_C, the object to be inspected. The conductivity and permeability of the flaw are different than those of the host material, thus the electromagnetic fields in the flawed arrangement satisfy

$$\begin{array}{ll} \operatorname{curl} \mathbf{H}^f - \boldsymbol{\sigma}^f \mathbf{E}^f = \mathbf{J}_e & \text{in } \Omega \\ \operatorname{curl} \mathbf{E}^f + i\omega \boldsymbol{\mu}^f \mathbf{H}^f = \mathbf{0} & \text{in } \Omega\,, \end{array}$$

where the superscript f denotes the quantities when the flaw is present. For the sake of simplicity, in the following we assume that the permeability is the same in the unflawed and flawed arrangements, and that the conductivity of the flaw is equal to 0, while outside it coincides with $\boldsymbol{\sigma}^u$, namely,

$$\boldsymbol{\sigma}^f = \begin{cases} \boldsymbol{\sigma}^u & \text{in } \Omega_C \setminus \Omega_f \\ \mathbf{0} & \text{in } \Omega_f\,. \end{cases}$$

We also set $\boldsymbol{\mu} := \boldsymbol{\mu}^f = \boldsymbol{\mu}^u$ and $\boldsymbol{\sigma} := \boldsymbol{\sigma}^u$. Hence when the flaw is present the impedance is given by

$$Z^f = \frac{1}{|I^0|^2} \left(\int_{\Omega_C \setminus \Omega_f} \boldsymbol{\sigma} \mathbf{E}^f \cdot \overline{\mathbf{E}^f} + i\omega \int_{\Omega} \boldsymbol{\mu} \mathbf{H}^f \cdot \overline{\mathbf{H}^f} \right). \tag{9.13}$$

The direct approach computes the difference between the impedance values with and without flaws, determined as in (9.12) and (9.13). The change of the observed quantity is very small, usually under 1% of the unflawed impedance value, so very high accuracy is needed in the finite element approximation of the fields. Sometimes the unperturbed configuration has symmetries that make it possible to simplify the computation, however the approximation of the perturbed problem requires a very fine three-dimensional mesh and can be extremely expensive for complicated geometrical situations.

In order to minimize this computational cost a different approach is based on perturbation techniques, that lead to the computation of the impedance variation as an integral on the flaw, thus making it possible to obtain sufficiently high accuracy by refining

the mesh only in the suspect region. These techniques can be described as follows. The computational domain Ω is assumed to have a simply-connected boundary $\partial\Omega$, and to be given by $\Omega = \Omega_C \cup \Omega_{\rm coil} \cup \Omega_I$, where the conductive coil $\Omega_{\rm coil}$ is an absolute probe, with two contacts $\partial\Omega_{\rm coil} \cap \partial\Omega = \Gamma_E \cup \Gamma_J$. The excitation is given by a current intensity I^0 (and not by a current density as in (9.11)). From the Ampère law, this assigned current intensity can be expressed as $I^0 = \int_{\Gamma_J} \operatorname{curl} \mathbf{H}^f \cdot \mathbf{n} = \int_{\Gamma_J} \operatorname{curl} \mathbf{H}^u \cdot \mathbf{n}$. Finally, let us also assume that the no-flux boundary conditions

$$\begin{aligned} &\mathbf{E}^u \times \mathbf{n} = \mathbf{0} \ \text{ on } \Gamma_E \cup \Gamma_J \\ &\boldsymbol{\mu}\mathbf{H}^u \cdot \mathbf{n} = 0 \ \text{ on } \partial\Omega \end{aligned}$$

are satisfied (see (8.2)).

For each $\mathbf{v} \in H(\operatorname{curl}; \Omega)$ such that $\operatorname{curl} \mathbf{v} = 0$ in $\Omega \setminus (\overline{\Omega_C} \cup \overline{\Omega_{\rm coil}})$ one has, as in Section 8.1,

$$\begin{aligned} -i\omega \int_\Omega \boldsymbol{\mu}\mathbf{H}^u \cdot \overline{\mathbf{v}} &= \int_\Omega \operatorname{curl} \mathbf{E}^u \cdot \overline{\mathbf{v}} \\ &= \int_\Omega \mathbf{E}^u \cdot \operatorname{curl} \overline{\mathbf{v}} - \int_{\partial\Omega} \mathbf{E}^u \times \mathbf{n} \cdot \overline{\mathbf{v}} \\ &= \int_{\Omega_C \cup \Omega_{\rm coil}} \boldsymbol{\sigma}^{-1} \operatorname{curl} \mathbf{H}^u \cdot \operatorname{curl} \overline{\mathbf{v}} - V^u \int_{\Gamma_J} \operatorname{curl} \overline{\mathbf{v}} \cdot \mathbf{n} \,. \end{aligned} \tag{9.14}$$

Analogously, assuming that also when the flaw is present the electromagnetic fields satisfy no-flux boundary conditions, one finds

$$\begin{aligned} -i\omega \int_\Omega \boldsymbol{\mu}\mathbf{H}^f \cdot \overline{\mathbf{v}} &= \int_\Omega \operatorname{curl} \mathbf{E}^f \cdot \overline{\mathbf{v}} \\ &= \int_\Omega \mathbf{E}^f \cdot \operatorname{curl} \overline{\mathbf{v}} - \int_{\partial\Omega} \mathbf{E}^f \times \mathbf{n} \cdot \overline{\mathbf{v}} \\ &= \int_{(\Omega_C \setminus \Omega_f) \cup \Omega_{\rm coil}} \boldsymbol{\sigma}^{-1} \operatorname{curl} \mathbf{H}^f \cdot \operatorname{curl} \overline{\mathbf{v}} \\ &\qquad + \int_{\Omega_f} \mathbf{E}^f \cdot \operatorname{curl} \overline{\mathbf{v}} - V^f \int_{\Gamma_J} \operatorname{curl} \overline{\mathbf{v}} \cdot \mathbf{n} \,. \end{aligned} \tag{9.15}$$

Taking $\mathbf{v} = \overline{\mathbf{H}^f}$ in (9.14) and $\mathbf{v} = \overline{\mathbf{H}^u}$ in (9.15), and recalling that $I^0 = \int_{\Gamma_J} \operatorname{curl} \mathbf{H}^f \cdot \mathbf{n} = \int_{\Gamma_J} \operatorname{curl} \mathbf{H}^u \cdot \mathbf{n}$, one has

$$V^u I^0 = \int_{\Omega_C \cup \Omega_{\rm coil}} \boldsymbol{\sigma}^{-1} \operatorname{curl} \mathbf{H}^u \cdot \operatorname{curl} \mathbf{H}^f + i\omega \int_\Omega \boldsymbol{\mu}\mathbf{H}^u \cdot \mathbf{H}^f$$

and

$$\begin{aligned} V^f I^0 = &\int_{\Omega_f} \mathbf{E}^f \cdot \operatorname{curl} \mathbf{H}^u + \int_{(\Omega_C \setminus \Omega_f) \cup \Omega_{\rm coil}} \boldsymbol{\sigma}^{-1} \operatorname{curl} \mathbf{H}^f \cdot \operatorname{curl} \mathbf{H}^u \\ &+ i\omega \int_\Omega \boldsymbol{\mu}\mathbf{H}^f \cdot \mathbf{H}^u \,, \end{aligned}$$

hence

$$\begin{aligned} (V^f - V^u) I^0 &= \int_{\Omega_f} \mathbf{E}^f \cdot \operatorname{curl} \mathbf{H}^u - \int_{\Omega_f} \boldsymbol{\sigma}^{-1} \operatorname{curl} \mathbf{H}^u \cdot \operatorname{curl} \mathbf{H}^f \\ &= \int_{\Omega_f} \mathbf{E}^f \cdot \operatorname{curl} \mathbf{H}^u \,, \end{aligned}$$

since $\operatorname{curl} \mathbf{H}^f = \mathbf{0}$ in Ω_f.

Proceeding as in (8.9) and taking into account the relations (9.12) and (9.13) we see that $Z^u = V^u/I^0$ and $Z^f = V^f/I^0$, hence the impedance variation is given by

$$(Z^f - Z^u) = \frac{V^f - V^u}{I^0} = \frac{1}{(I^0)^2} \int_{\Omega_f} \mathbf{E}^f \cdot \operatorname{curl} \mathbf{H}^u \, .$$

For the finite element approximation different formulations have been considered. More often the problem is formulated in terms of a magnetic vector potential $\mathbf{A}_C$ and an electric scalar potential V_C in the conductor, and a magnetic scalar potential ψ_I in the insulator (see Section 6.3). The first three-dimensional simulations, due to Ida and Lord [136], use this formulation and isoparametric hexahedral finite elements for the approximation of the impedance, given a source current density $\mathbf{J}_e$. They verify the validity of the formulation for a problem related to the non-destructive testing of a nuclear plant steam generator. In particular, the test problem consists of an Inconel 600 (a nickel-chromium allotrope of iron) tube and a carbon steel support plate; two conical defects are located on the outer surface of the tube.

Rasolonjanahary et al. [204] consider the problem of the inspection of flaws in a riveted aircraft structure. They use a $(\mathbf{A}_C, V_C)$ formulation in the conductor to be inspected and the magnetic scalar potential ψ_I in the surrounding non-conducting region. They compare the results obtained using in the flaw domain a formulation in terms of either the vector magnetic potential $\mathbf{A}$ or the scalar magnetic potential ψ, and obtain more accurate results with the former formulation.

Badics et al. [33] use perturbation techniques in terms of the vector potential $\mathbf{A}_C$ and the electric scalar potential V_C in the conductor, the vector magnetic potential $\mathbf{A}$ in the flaw and the magnetic scalar potential ψ_I in the air region. They compute the solution of the unperturbed model and the field distortion due to a flaw. Setting $\mathbf{H} := \mathbf{H}^f - \mathbf{H}^u$ and $\mathbf{E} := \mathbf{E}^f - \mathbf{E}^u$ in Ω and assuming as before that the permeability is the same in the unflawed and flawed arrangements and that the conductivity of the flaw is equal to 0, one has

$$\begin{aligned} &\operatorname{curl} \mathbf{H} - \boldsymbol{\sigma}^f \mathbf{E} = \mathbf{J}_* \quad &&\text{in } \Omega \\ &\operatorname{curl} \mathbf{E} + i\omega\boldsymbol{\mu}\mathbf{H} = \mathbf{0} \quad &&\text{in } \Omega \, , \end{aligned}$$

where

$$\mathbf{J}_* := (\boldsymbol{\sigma}^f - \boldsymbol{\sigma})\mathbf{E}^u = \begin{cases} \mathbf{0} & \text{in } \Omega \setminus \Omega_f \\ -\boldsymbol{\sigma}\mathbf{E}^u & \text{in } \Omega_f \, . \end{cases}$$

Hence, for calculating the impedance perturbation it is necessary to know the value of the unflawed electromagnetic fields only in the flaw.

The efficiency of the formulation is verified by solving the TEAM workshop problem 15 (see Figure 9.27 for a sketched description of the arrangement). The test specimen is an aluminum alloy plate of 260 mm of side (2d) and 12.22 mm of thickness (t). The defect is a parallelepipedal slot of length 12.60 mm (2c), depth 5 mm (h) and width 0.28 mm (w). The probe is a circular air-cored coil with inner radius 9.34 mm, outer radius 18.40 mm and 9 mm of length. The frequency of the applied current is equal to 7 kHz and the lift-off of the probe is 2.03 mm.

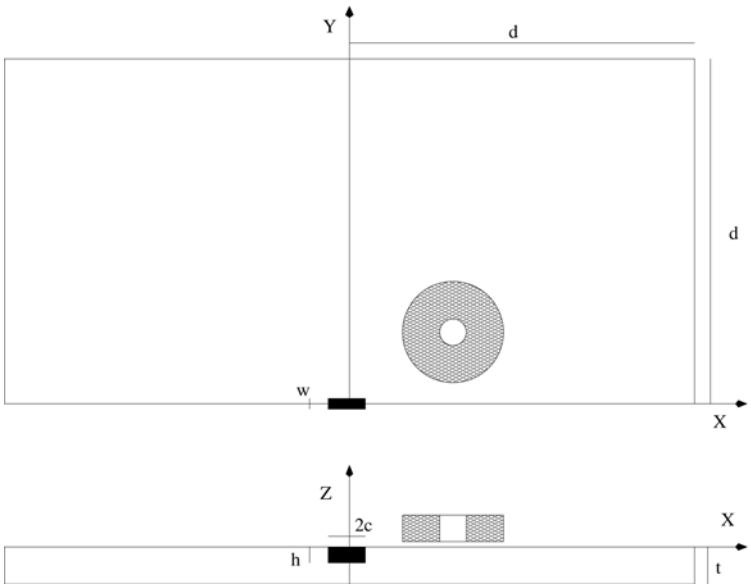

Fig. 9.27. Sketch of problem 15 of the TEAM workshop

They also solve two other test problems where the host specimen is a stainless steel tube and the probe is again a circular air-cored coil. The defect is a long axial slot in the first case and a short circumferential slot in the second case.

Sabariego and Dular [214], [215] propose a perturbation approach using the **H**-based formulation and edge finite elements for its numerical approximation. The perturbed field is not computed in the whole domain but only in a reduced domain surrounding the flaw. The mesh of this reduced subdomain is independent of the mesh used for the unflawed problem and can be adapted to the dimensions of the flaw. To demonstrate the performance of the proposed method they consider the second eddy current benchmark problem proposed by the World Federation of NDE Centers, an Inconel tube with a defect on the outer surface and a circular coil that scans the inner surface.

In Henneron et al. [125] the $(\mathbf{A}, V_C)$ formulation and the $(\mathbf{T}_C, \psi)$ formulation are considered, and are compared in terms of numerical results and computational time. The numerical experiments concern the qualification process of testing devices used in heat exchanger tubes. Two different probes are considered. The first one consists in two coils with a ferrite core used as source and receptive coils, simultaneously. The second one has a source coil and two different receptive coils. Also Krebs et al. [156] use these two formulations to obtain a-posteriori error estimators within an adaptive meshing procedure.